# Scrape-off Layer Plasma Flow in L- and H-Mode Plasmas on JT-60U*⁾

Nobuyuki ASAKURA

*Japan Atomic Energy Agency, Naka, Ibaraki 311-0193 Japan*

Significant progress has been made in understanding the scrape-off layer (SOL) mass transport along magnetic field lines—the SOL flow. Understanding the driving mechanisms of the SOL flow was summarized based on experiments in the JT-60U tokamak plasmas. Fast SOL flow with parallel Mach numbers of 0.2-1 was generated from the low magnetic field side (LFS) SOL to the high magnetic field side (HFS) divertor for the ion $\nabla B$ drift direction toward the divertor. The SOL flow pattern was formed mainly by the LFS enhanced in-out asymmetry in diffusion and by classical drifts in the torus. Detachment of the divertor plasma affected enhancement of the SOL flow at the HFS SOL. Dynamics of the SOL flow were measured during the transient event of edge localized modes (ELM), and the flow pattern of the plasma filaments was clarified at both SOLs. The radial movement of the ELM filaments at the LFS SOL was sometimes faster than the parallel convective transport to the divertor target, which caused the heat loading to the first wall. Filament structures with temporal peaks and flow velocities comparable to the ion sonic level were also determined in the HFS SOL, but they appeared only near the separatrix. The delay after start of the ELM was shorter than the parallel convection time from the LFS midplane, suggesting that part of the ELM filaments was ejected into the HFS SOL.

## 1. Introduction

The scrape-off layer (SOL) plasma flow along magnetic field lines (SOL flow) is of direct relevance to particle control, in terms of the divertor pumping and impurity screening properties. In the simple SOL model, the SOL flow is generated toward the divertor target by the parallel gradient of plasma pressure, while the Mach number is small ($M_{//} < 0.1$), except in the vicinity of the divertor sheath. In many tokamak experiments and modeling work, significant progress has been made in understanding the SOL mass transport mechanisms. Multi-point measurements of the SOL flow in L- and H-mode plasmas showed that subsonic to sonic levels of the parallel Mach number ($M_{//} = 0.2$-$1$) were generated from the low magnetic field side (LFS) SOL to the high magnetic field side (HFS) divertor for the ion $\nabla B$ drift direction toward the divertor [1–10]. Such SOL flow patterns were produced by a combination of the driving mechanisms, i.e., mainly produced by the in-out asymmetry in diffusion enhanced at the LFS and by classical drifts in the torus. At the same time, the divertor plasma detachment increased the flow velocity.

Significant heat and particle fluxes are loaded to the divertor target during the transient event (of a few $100\,\mu s$) of the edge localized mode (ELM) [11,12]. Therefore, amplitude reduction is crucial for operation of the Interna-tional Thermonuclear Experimental Reactor (ITER). Investigation of the SOL filament dynamics has been progressed through the use of fast TV cameras for visible and infrared images, and probe measurements [13]. Time evolutions of the plasma filaments with temporal multi-peaks in ion-saturation signals were determined at SOL [9, 12, 14], and the sonic level of the SOL flow, i.e., $C_s = \sqrt{((T_i + T_e)/m_i)}$ was determined at the HFS and LFS. Depositions of the large heat and particle fluxes on the LFS target occur with the characteristic time of plasma convection—several $10\,\mu s$ to a few $100\,\mu s$ [11]. On the other hand, it was found that the flow patterns in the ELM filaments differed between the LFS and HFS SOLs, which potentially affects the deposition profiles of the transient heat and particle fluxes and impurity generation at the target.

This paper presents the flow pattern at both the HFS and LFS SOLs in the steady-state and transient period of the ELM deposition. Change in the SOL flow profile, along and across the magnetic field lines, and the SOL flow driving mechanisms, are reviewed in Secs. 2 and 3, respectively, based on experiments in the L-mode plasma with the JT-60U tokamak. Recent understanding of the transient flow patterns at the LFS and HFS SOLs is summarized in Sec. 4. The summary and conclusions are presented in Sec. 5.

---

*author's e-mail: Asakura.nobuyuki@jaea.go.jp*

## 2. Scrape-off Layer Flow in L-mode
### 2.1 Measurement of parallel plasma flow

SOL flow measurements, mostly in L-mode plasmas on the JT-60U, were taken with Mach probes at three different poloidal locations: LFS midplane, near the null-point (X-point), and above the HFS baffle. $M_{//}$ is calculated from the ratio of the ion saturation currents at the electron and ion sides ($j_s^e$ and $j_s^i$), using Hutchinson's formula [15]: $M_{//} = \alpha ln[j_s^e / j_s^i]$, where $\alpha = 0.35$ for the collisional SOL plasma condition. Here, main plasma parameters are $I_p = 1\,\text{MA}$, $B_t = 3.3\,\text{T}$, $P_{NB} = 4\,\text{MW}$.

Figure 1 shows the radial profiles of $M_{//}$ with the ion $\boldsymbol{B} \times \nabla B$ drift direction toward the divertor, where the radial coordinate of profiles is mapped at the LFS midplane ($r^{\text{mid}}$). Positive and negative directions indicate par-
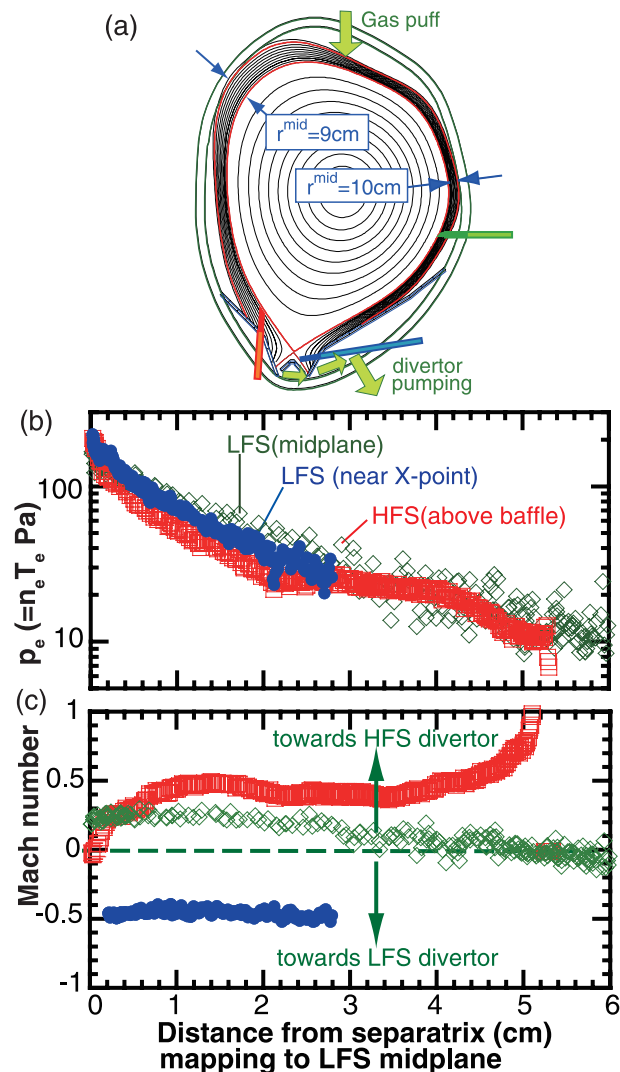


Fig. 1 (a) Standard plasma configuration and Mach probe locations (at LFS midplane, just below X-point, above HFS baffle). Profiles of (b) electron pressure, (b) Mach number measured by three Mach probes for the ion $\nabla B$ drift direction towards the divertor. Positive value presents the SOL flow towards the HFS divertor.

allel flow toward the HFS and LFS divertors, respectively. Plasma electron pressures at the different locations are comparable on the magnetic surfaces. On the other hand, flow pattern changed: SOL flow away from the LFS divertor (toward the plasma top, i.e., opposite to what one would expect from the simple picture) occurs in the wide region at the LFS midplane ($r^{\text{mid}} < 5\,\text{cm}$), and $M_{//}$ becomes subsonic ($M_{//} = 0.3\text{-}0.4$). Considering the Joint European Torus (JET) result at the plasma top [6], the fast SOL flow is continuously toward the HFS SOL, and the radial location of the maximum $M_{//}$ extends to the outer flux surfaces (far SOL). At the HFS SOL, the maximum $M_{//}$ increased to a sonic level (from 0.5 to larger than 1) [5, 7], whereas measurements of $M_{//}$ in the narrow region near the separatrix show no (in the Alcator C-MOD) or small flow toward the plasma top ($M_{//} = -0.1$ to 0 in the JT-60U). The SOL flow pattern was basically similar between transient ELM events in H-mode plasmas [9, 12, 14].

In the standard tokamak operations, all results are consistent with the fact that subsonic SOL flow is produced from the LFS SOL to the HFS divertor for the ion $\boldsymbol{B} \times \nabla B$ drift direction toward the divertor, independent of the divertor geometry. On the other hand, in the LFS divertor and near the X-point, SOL flow toward the LFS divertor target was observed [3, 4, 14], suggesting that the *stagnation point* is between the LFS midplane and the LFS SOL near the X-point.

It was also found that the SOL flow direction at the LFS midplane reversed for ion $\boldsymbol{B} \times \nabla B$ drift away from the divertor, i.e., an SOL flow was generated opposite to the ion $\boldsymbol{B} \times \nabla B$ drift direction, and the SOL flow toward the HFS divertor was sustained and rather enhanced at the HFS. This suggests that there exists at least two driving mechanisms: (i) A $B_t$-independent component of the SOL flow is produced toward the HFS SOL, and (ii) a $B_t$-dependent component appears in opposition to the ion $\boldsymbol{B} \times \nabla B$ drift. A combination of driving mechanisms forms the complicated SOL flow pattern.

### 2.2 Plasma pressure enhancement at the LFS

To understand the driving mechanism of the $B_t$-independent SOL flow component, SOL plasma measurement was performed in a special plasma configuration with small separation between the upper-inner first wall and the separatrix, as shown in Fig. 2 (a), where an SOL connected between the HFS and LFS divertors is within the 2.4 cm midplane radius. Profiles of electron pressure ($p_e = n_e T_e$) at the HFS SOL and the LFS midplane are comparable with that of the in-out connected SOL. On the other hand, $p_e$ at the HFS SOL is reduced in the separated SOL ($r^{\text{mid}} > 2.5\,\text{cm}$) compared to that at the LFS midplane, where connection lengths from the upper-inner wall to the two Mach probes are comparable, i.e., $L_c = 50$ and $40\,\text{m}$ to the HFS and midplane Mach probes, respectively. The
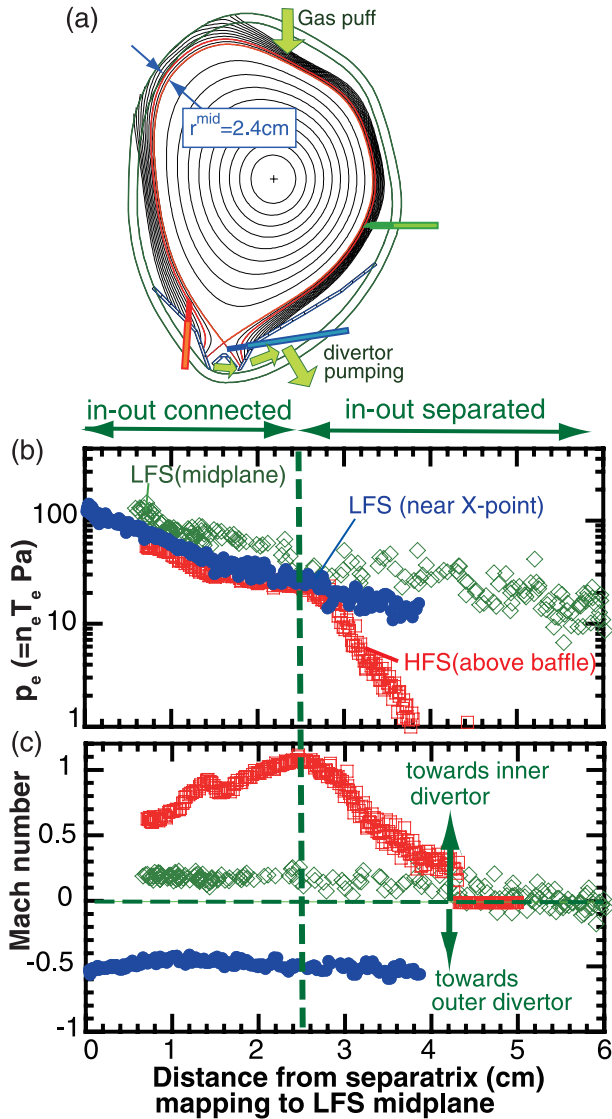
Fig. 2  (a) Plasma configuration with small separation between the upper-inner first wall and separatrix ($r^{mid}$ = 2.4 cm). Profiles of (b) electron pressure, (b) Mach number measured by three Mach probes.



Fig. 3  SOL flow profiles at LFS midplane at low and medium densities ($n_e/n^{GW}$ = 0.2-0.24 and 0.44-0.46) are presented by closed and open symbols. Positive value shows the direction towards the HFS divertor. Squares and circles for the ion $\boldsymbol{B} \times \nabla B$ drift direction towards and away from the divertor, respectively.

distribution as well as $T_e$ and the in-out asymmetry in the radial diffusion in SOL will determine the driving mechanism of the $B_t$-independent SOL flow component more quantitatively.

## 2.3   Drift effects in a tokamak

Figure 3 shows $M_{//}$ profiles at the LFS midplane with increasing $\bar{n}_e/n^{GW}$ from low (0.2-0.24) to medium (0.44-0.46) values for the ion $\boldsymbol{B} \times \nabla B$ drift direction toward and away from the divertor. Results at the LFS midplane show two general characteristics of the $B_t$-dependent component of the SOL flow: 1) The direction of the SOL flow changes with the $B_t$ reversal (the SOL flow direction in poloidal projection at the midplane is against the ion $\boldsymbol{B} \times \nabla B$ drift direction). 2) The absolute value of maximum $M_{//}$ decreases from 0.4 to 0.1-0.2 with increasing $\bar{n}_e$.

Effects of classical drifts in SOL [16, 17] are candidates for the $B_t$-dependent component. The classical drifts such as $\boldsymbol{E} \times \boldsymbol{B}$ and $\boldsymbol{B} \times \nabla B$ (and diamagnetic, $\nabla p \times B$, for fluid model) play an important role in perpendicular and parallel transport in toroidal geometry [18,19]. In the SOL, parallel flow, i.e., ion Pfirsch-Schlüter (PS) flow, can be produced due to the in-out asymmetry of $E_r \times B$ and $\nabla p_i \times B$ drifts in the flux surfaces for the fluid model. Poloidal projections of the ion PS flow—$E_r \times B$, $\nabla p_i \times B$, and ion $\boldsymbol{B} \times \nabla B$ drifts are illustrated in Fig. 4. The PS flow is against the ion $\boldsymbol{B} \times \nabla B$ drift, and the theoretical formula in a confined plasma, $V_{//}^{PS} = 2q_s V_\perp \cos\theta$ ($q_s$ is the safety factor, $\theta$ is poloidal angle, $V_\perp = [E_r - \nabla p_i/en_i]/B$ where $E_r \times B$ and $-\nabla p_i \times B$ are basically the same direction in SOL) has a maximum at the midplane.

Simple evaluation of $V_{//}^{PS}$ from measured $T_i$, $T_e$, and $V_f$ profiles was done at the LFS midplane for normal and reversed $B_t$ cases in JT-60U [18] and TCV [8]. Mach numbers ($V_{//}^{PS}/C_s$) and the reduction with increasing $\bar{n}_e$, due to reduction in $E_r$ and $\nabla p_i$ at high $\bar{n}_e$, were consistent with the

sonic level of the SOL flow at the HFS SOL is also reduced in the separated SOL, as shown in Fig. 2 (c).

As a result, for the in-out connected SOL for the single null divertor, the dominant particle transport in the HFS SOL is produced by the parallel flow from the LFS rather than the transverse transport—a large part of the HFS SOL plasma is transported from the LFS SOL. Similar results of in-out asymmetry in the plasma pressure in the separated SOL and stagnation of the SOL flow at HFS SOL were demonstrated in the double null divertor configuration on Alcator C-mod [7]. Generally, in the connected SOL, the static pressure component ($n_e T_e + n_i T_i$) plus the dynamic pressure component ($m_i n_i [M_{//}/C_s]^2$) should be balanced along the field line, assuming no pressure/momentum source nor loss in the SOL. In future, measurements of $T_i$
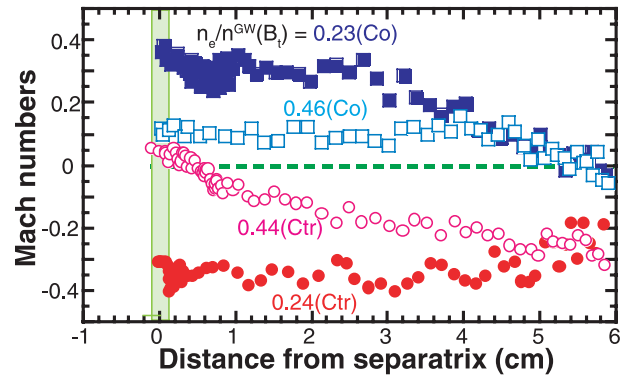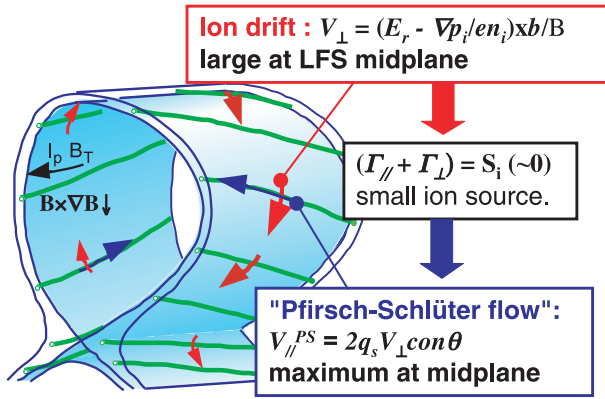
Fig. 4    Directions of the poloidal drift velocity, and parallel SOL flow "Pfirsch-Schlüter flow" for the ion $B \times \nabla B$ drift direction towards the divertor.



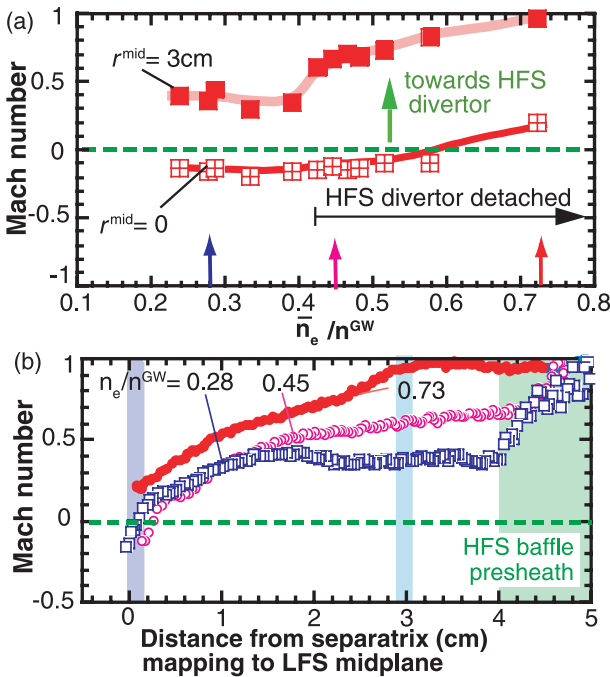Fig. 5    (a) $M_{//}$ above the HFS baffle for $r^{mid} = 0$ and 3 cm as a function of $n_e/n^{GW}$. (b) SOL flow profiles in density scan (circles and squares are attached and detached HFS divertors, respectively) for normal and reversed $B_t$ cases.

Mach probe measurements. Thus, the general characteristics of the $B_t$-dependent flow can be explained by the PS flow, but its influence in the open field line may be smaller than the simple formula of $V_{//}^{PS}$ on the closed flux surface.

## 2.4   Influence of divertor detachment

Detachment of the divertor plasma causes momentum loss and thus modifies the pressure balance. Figure 5 shows the change in the $M_{//}$ profile above the HFS baffle with increasing $\bar{n}_e$. When the plasma detachment occurs at the HFS divertor, the $M_{//}$ profile changes: $M_{//}$ at far SOL

is enhanced and finally reaches a sonic level during the X-point MARFE at $\bar{n}_e/n^{GW} = 0.85$. Here, $T_e$ values near the HFS SOL separatrix ($T_e^{sep}$) and at the far SOL ($T_e^{far}$ at $r^{mid} \sim 3$ cm) decrease from 90 to 45 eV, and from 27 to 20 eV, and $C_s^{sep}$ and $C_s^{far}$ decrease from 94 to 67 kms$^{-1}$, and from 52 to 45 kms$^{-1}$ respectively. Thus, the enhancement of $M_{//}$ at far SOL is generated by an increase in $V_{//}^{far}$ rather than a reduction in $C_s^{far}$. On the other hand, $n_e$ and $p_e$ increase at the LFS midplane, while $M_{//}$ (and $m_i n_i [M_{//}/C_s]^2$) decreased slightly, as shown in Fig. 3. Thus, the total pressure at the LFS midplane is maintained or rather increased. As a result, a large enhancement of the HFS SOL flow (particularly the $B_t$-independent flow) up to the sonic level is caused by detachment at the HFS divertor, in addition to increasing the plasma pressure at LFS SOL. In C-MOD, a sonic level of $M_{//}$ is generally observed, even at the HFS midplane [7], which may be due to the HFS divertor detachment.

## 3.   Transient SOL Flow during ELM

Understanding of edge and SOL plasma dynamics during ELM has recently progressed through the use of time-resolving diagnostics, such as fast TV cameras for visible and infrared images, Langmuir probes, and fast Bremsstrahlung-Emission-Spectroscopy (BES) [20–28]. In particular, evolution of ELM filaments is of great interest for understanding heat and particle transport to plasma facing components (PFC) such as the divertor and the first wall. Plasma filaments with multiple temporal peaks in ion-saturation signals were determined in many tokamak experiments [12–14, 26, 28], and the transient plasma flows in the filaments, as well as the convective ELM plasma flux, affect heat and particle loading on the PFCs and impurity transport. This section focuses on the transient SOL flow patterns caused by ELM at both the HFS and LFS SOLs.

### 3.1   Transient flow at the LFS midplane and divertor

Figure 6 shows the expanded time evolutions of $D_\alpha$ brightness at the LFS divertor and ion-saturation signals at the LFS midplane and the X-point ($j_s^{mid}$ and $j_s^{Xp}$), where the midplane Mach probe is located at $z = -40$ cm below the plasma equatorial plane ($z = 0$). The data sampling time is 2 μs. An ELM event occurs when the Mach probes are near the separatrix and the temporal evolution is shown as delay from the ELM start, determined by a large turbulence of the magnetic pickup probes. Here, main plasma parameters are $I_p = 1$ MA, $B_t = 1.86$ T, $P_{NB} = 5$ MW.

Multiple large positive peaks are observed from the two sides of the midplane Mach probe in Fig. 6 (b), which indicates that ejected ELM filaments extend to the Mach probe location along magnetic field lines. The delays of three representative peaks at the midplane-side $j_s^{mid}$ are $\tau^{mid}$(peak) = 9, 25, and 53 μs. The second and third peaks
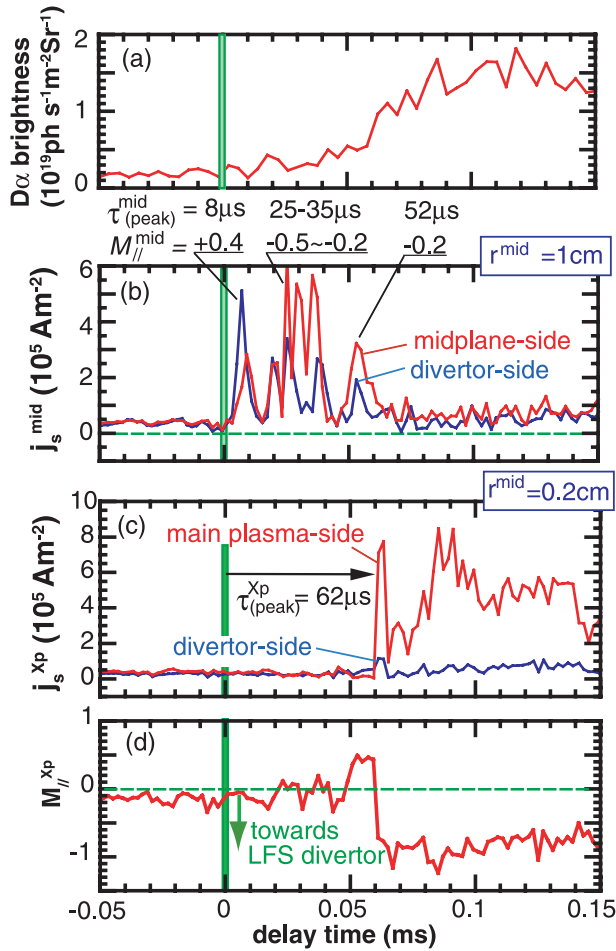
Fig. 6 Enlarged time evolution signals during an ELM event: (a) $D_\alpha$ brightness at the outer divertor, (b) $j_s^{mid}$ at midplane-side and LFS divertor-side of the midplane Mach probe, (c) $j_s^{Xp}$ at main plasma-side and divertor-side of the X-point Mach probe, (d) evaluated Mach numbers. Corresponding radii at the midplane ($r^{mid}$) are 1 and 0.2 cm. Delay from the ELM start (large magnetic turbulence) is shown as horizontal axis.
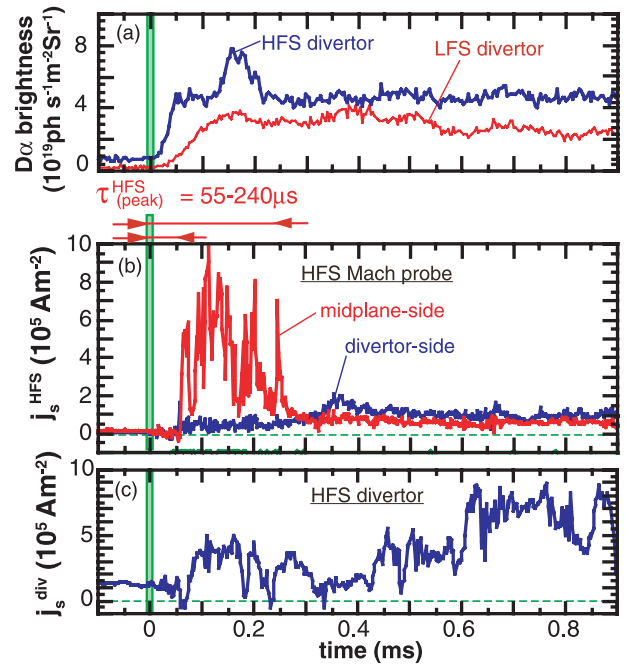


Fig. 7 Time evolutions of (a) $D_\alpha$ brightness in the LFS and HFS divertors, (b) ion saturation currents, $j_s$, at the midplane- and divertor-sides of the HFS Mach probe ($r^{mid} = 0.3$ cm), (c) $j_s$ at the HFS divertor strike-point ($r^{mid} = 0.3$ cm), as a function of delay from the start of large magnetic turbulence.

($\sim 5.7 \times 10^5$ and $\sim 3.2 \times 10^5$ Am$^{-2}$) are larger than the first peak ($2.5 \times 10^5$ Am$^{-2}$). Corresponding peaks in the divertor side $j_s^{mid}$ are observed at $t = 7$, 25, and 51 µs, and the first peak ($6 \times 10^5$ Am$^{-2}$) is larger than the other peaks ($3.2 \times 10^5$, $2.2 \times 10^5$ Am$^{-2}$). As a result, $M_{//}^{mid} = +0.4$, $-0.2$ to $-0.5$, $-0.2$, where only the first peak is away from the LFS divertor. After the appearance of the peaks, both side $j_s^{mid}$ values are comparable ($0.5$-$0.8 \times 10^5$ Am$^{-2}$), and $M_{//}^{mid} = -0.2$ to 0.

Near the X-point, the first large $j_s^{Xp}$ peak is observed at $\tau^{Xp}(peak) = 62$ µs, as shown in Fig. 6 (c)—in particular, at the main plasma side of the Mach probe, then, the $j_s^{Xp}$ base level increases to a comparable value at $t = 85$-$93$ µs. At the same time, the parallel convection transport toward the LFS divertor with a sonic velocity becomes dominant, as shown in Fig. 6 (d), and the delay of the first $j_s^{Xp}$ peak from the ELM start is comparable to

the characteristic convection time of the pedestal plasma—$\tau_{//}^{conv} = L_c^{mid\text{-}Xp}/C_s^{ped} = 23 \, m / 300 \, kms^{-1} = 77 \, µs$, where $C_s^{ped} = \sqrt{((T_i^{ped} + T_e^{ped})/m_i)}$, $T_i^{ped} = 1.2$ keV, $T_e^{ped} = 0.9$ keV.

Here, multiple peaks in $j_s^{Xp}$ are not often observed, and delays of the early peaks ($\tau^{Xp}(peak) = 62$ and 85-93 µs) are comparable to $\tau_{//}^{conv}$, thus it is difficult to determine the ELM filaments and the convective transport of the ELM plasma. It was shown that the radial movement of the ELM filaments (in particular, the first few of the multiple peaks) at the LFS SOL has a high velocity of $V_\perp^{mid} = 0.4$-$3$ kms$^{-1}$, and that the radial transport time to the first wall is often faster than the characteristic time of the parallel convective transport to the divertor [29]. This potentially causes the heat loading to the first wall.

### 3.2 Transient SOL flow at the HFS SOL

During ELM events, heat and particle fluxes are deposited to the HFS and LFS divertor targets almost simultaneously. This suggests that the ELM plasma transport to the HFS target is faster than the convection time from the LFS midplane to the HFS divertor. Figure 7 shows the time evolution of $D_\alpha$ brightness at the HFS and LFS divertors, $j_s$ at the midplane and divertor sides of the HFS Mach probe ($j_s^{HFS\text{-}mid}$ and $j_s^{HFS\text{-}div}$) and $j_s$ at the HFS strike point ($j_s^{HFS\text{-}div}$) during an ELM event, which is a different time, as shown in Fig. 6. The local distance from the separatrix

to the Mach probe is 1.1 cm, which corresponds to just outside the separatrix when mapped along the flux surface to the LFS midplane ($r^{\mathrm{mid}} = 0.3$ cm).

It is found that multiple peaks appear in $j_s^{\mathrm{HFS\text{-}mid}}$ with delays of 55-240 μs after the start of the ELM event. On the other hand, the large peak is not observed in $j_s^{\mathrm{HFS\text{-}div}}$, although $j_s^{\mathrm{HFS\text{-}div}}$ does increase after $t = 55$ μs. This indicates that some convection flux (with the sonic level of the parallel velocity) reach the HFS SOL more rapidly than the characteristic convection time from the LFS midplane to the Mach probe—$\tau_{//}^{\mathrm{conv}} = L_c^{\mathrm{LFS\text{-}HFSprobe}}/C_s^{\mathrm{ped}} = 50$ m/$300$ kms$^{-1}$ ~ $167$ μs. During the $j_s^{\mathrm{HFS}}$ increase, $j_s$ at the HFS strike point ($j_s^{\mathrm{div\text{-}HFS}}$) also increases, but again a large peak is not observed, similar to the LFS X-point and divertor target.

During the later period of $j_s^{\mathrm{HFS}}$ enhancement ($t = 0.3$-$1$ ms), $j_s^{\mathrm{HFS\text{-}div}}$ becomes larger than $j_s^{\mathrm{HFS\text{-}mid}}$, which shows that the SOL plasma flow from the HFS divertor occurs above the HFS baffle. The flow reversal can be explained by large increases in the particle recycling and the plasma pressure at the HFS divertor after large particle flux of the ELM filaments is transported to the HFS divertor.

## 3.3 Transient SOL flow pattern at LFS and HFS

Radial distributions of $j_s^{\mathrm{mid}}$ peaks, $j_s^{\mathrm{mid}}$(peak), and $j_s^{\mathrm{mid}}$ between ELM events, $j_s^{\mathrm{mid}}$(ss), are shown in Fig. 8 (a). These distributions are deduced from four similar ELMy H-mode discharges; the $j_s^{\mathrm{mid}}$(peak) profile is an envelope of $j_s^{\mathrm{mid}}$ peaks rather than a profile appearing at one moment. Here, magnetic field lines at $r^{\mathrm{mid}} > 13$ cm are connected to the upper LFS first wall, while those between $3.3$ cm $< r^{\mathrm{mid}} < 13$ cm are connected to the LFS baffle. The values of the first $j_s^{\mathrm{mid}}$ peaks varied from $1 \times 10^5$ to $5.5 \times 10^5$ Am$^{-2}$ near the separatrix. The enhancement factor of $j_s^{\mathrm{mid}}$(peak) compared to $j_s^{\mathrm{mid}}$(ss) is 10-100 over a wide SOL region. Large enhancement of radial propagation of $j_s^{\mathrm{mid}}$(peak) is observed in the outer flux surfaces ($r^{\mathrm{mid}} > 2$ cm); its e-folding length ($\lambda_{\mathrm{peak}}^{\mathrm{mid}}$) of 7.5 cm is 2.4 times larger than that of $j_s^{\mathrm{mid}}$(ss) ($\lambda_{ss}^{\mathrm{mid}} = 3.1$ cm).

Radial distributions of $j_s^{\mathrm{Xp}}$ peaks, $j_s^{\mathrm{Xp}}$(peak), and $j_s^{\mathrm{Xp}}$ between ELM events, $j_s^{\mathrm{Xp}}$(ss), are shown in Fig. 8 (c), where the distributions are mapped to the midplane radius, and field lines for $r^{\mathrm{mid}} < 3.1$ cm are connected to the LFS divertor plates. The database of $j_s^{\mathrm{Xp}}$(peak) includes all peaks with the convective transport time scale, i.e., both the short peak shown at $t = 62$ μs and the large enhancement of $j_s^{\mathrm{Xp}}$ base level at $t = 85$-$93$ μs in Fig. 6 (c). In the flux surfaces near the separatrix ($r^{\mathrm{mid}} < 3$ cm), the enhancement factor of the $j_s^{\mathrm{Xp}}$(peak) is 10-100, which is comparable to that at the midplane. On the other hand, its e-folding length ($\lambda_{\mathrm{peak}}^{\mathrm{Xp}}$) of 1.3 cm is comparable to $\lambda_{ss}^{\mathrm{Xp}} = 1.5$ cm, but much smaller than $\lambda_{\mathrm{peak}}^{\mathrm{mid}}$ in the outer SOL at the midplane. These results suggest that some filaments with relatively small $V_\perp^{\mathrm{mid}}$ are transported to the divertor, while filaments
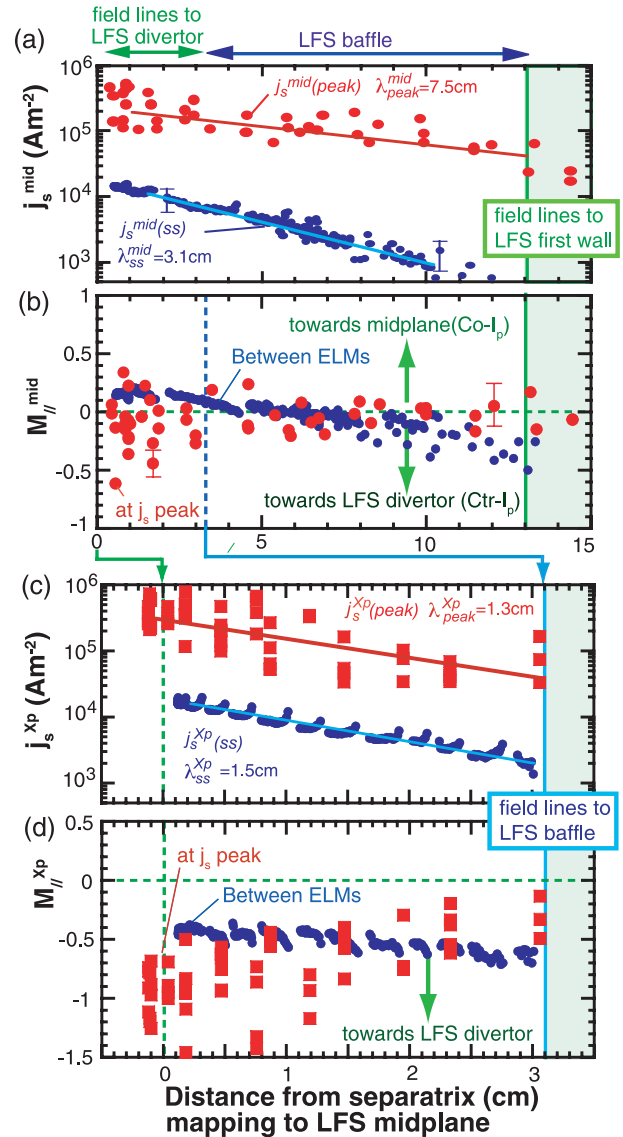


Fig. 8  Radial distributions of (a) $j_s^{\mathrm{mid}}$ peaks (red circles) during ELMs and $j_s^{\mathrm{mid}}$ between ELMs (blue circles) measured at midplane-side of the Mach probe, (b) Mach numbers corresponding to $j_s^{\mathrm{mid}}$(peak) and $j_s^{\mathrm{mid}}$(ss), (c) $j_s^{\mathrm{Xp}}$ peaks (red squires) measured near the X-point during ELMs and jsmid between ELMs (blue circles), (d) Mach numbers corresponding to $j_s^{\mathrm{Xp}}$(peak) and $j_s^{\mathrm{Xp}}$(ss). All profiles are mapped to the LFS midplane radius.

with large $V_\perp^{\mathrm{mid}}$ (larger than $r^{\mathrm{mid}}/\tau_{//}^{\mathrm{conv}} = 3$ cm/$77$ μs ~ $0.4$ kms$^{-1}$) propagate to the first wall or baffle.

Radial distributions of the Mach number at the midplane and near the X-point are shown in Figs. 8 (b) and (d), respectively. The values of $M_{//}^{\mathrm{mid}}$ are scattered between $-0.6$ and $+0.4$, and a subsonic level of the parallel flow is observed near the separatrix ($r^{\mathrm{mid}} < 2$ cm), often directed to the LFS divertor. The toroidal rotation velocity of the edge pedestal plasma is $V_t^{\mathrm{ped}} = 1 \times 10^5$ ms$^{-1}$ directed to the plasma current, while the measurement shows that parallel flow in number of filaments is produced in the counter $I_p$

direction. Thus, edge pedestal momentum in the filaments may be lost when they develop in the edge or are exhausted to the SOL region.

The convection SOL flow measured near the X-point dominates the sonic level, particularly in $r^{mid} < 1.5$ cm, whereas $M_{//}^{Xp}$ is a subsonic level in the outer flux surfaces. The convective ELM plasma, or some filaments with relatively small radial diffusion velocity, reach the divertor.

Next, the radial distributions of $j_s^{HFS\text{-}mid}$ peak values and $j_s^{HFS\text{-}mid}$ between ELMs, $j_s^{HFS}(ss)$, are shown in Fig. 9 (a), mapped to the LFS midplane radius. As presented in Sec. 3.2, very large multiple peaks, $j_s^{HFS}(peak)$, are often observed only near the separatrix ($r^{mid} < 0.6$ cm) in $j_s^{HFS\text{-}mid}$, as shown during $t = 55\text{-}240\,\mu s$ in Fig. 7 (b). The enhancement factors of $j_s^{HFS}(peak)$ are 20-50, which are comparable to those at the LFS midplane (10-100). On the other hand, in the outer flux surfaces ($r^{mid} > 1$ cm), very few such large $j_s^{HFS}$ peaks appear.

The maximum base level, $j_s^{HFS}(base)$, was observed over all radial locations after the convection transport time ($\tau_{//}^{conv} = L_c^{LFS\text{-}HFSprobe}/C_s^{ped} \sim 167\,\mu s$) and (near the separatrix) large peaks, as shown at $t \sim 350\,\mu s$ in Fig. 7 (b), appeared. The values of $j_s^{HFS}(base)$ are smaller than $j_s^{HFS}(peak)$ and the e-folding length of $j_s^{HFS}(base)$ mapped to the LFS midplane is $\lambda_{base}^{HFS} = 4.1$ cm, which is larger than $\lambda_{ss}^{HFS} = 1.1$ cm, but about a half that at the LFS midplane

($\lambda_{peak}^{mid} = 7.5$ cm).

The Mach numbers for $j_s^{HFS}(peak)$, $j_s^{HFS}(base)$, and $j_s^{HFS}(ss)$, are shown in Fig. 9 (b) as $M_{//}^{HFS}(peak)$, $M_{//}^{HFS}(base)$, and $M_{//}^{HFS}(ss)$, respectively. Here, $n_e$ in the SOL between ELMs (e.g., $n_e^{sep} \sim 4 \times 10^{18}$ m$^{-3}$ for $\bar{n}_e/n_{GW} = 0.46$) is smaller than that for the L-mode, as shown in Fig. 5 ($n_e^{sep} \sim 7 \times 10^{18}$ m$^{-3}$ for $\bar{n}_e/n_{GW} = 0.28$). Generally, $M_{//}^{HFS}(ss) = 0.1\text{-}0.3$ is smaller than that in the L-mode ($M_{//}^{HFS} = 0.3\text{-}0.4$). $M_{//}^{HFS}(peak)$ increases significantly toward the HFS divertor—in particular, nearing unity close to the separatrix. A sonic level of the fast SOL flow is produced only near the separatrix ($r^{mid} < 0.8$ cm), accompanied by large and short multiple peaks. This would cause the convective heat load near the HFS strike point.

Here, in Fig. 10, the delay of $j_s^{HFS}(peak)$, i.e., $\tau^{HFS}(peak)$, is compared to characteristic times of the convective transport from the LFS midplane, $\tau_{//}^{conv}(LFS\text{-}mid)$, and from the HFS midplane, $\tau_{//}^{conv}(HFS\text{-}mid)$, assuming $C_s^{ped}$ of $2.9 \times 10^5$ ms$^{-1}$, where the connection length varies slightly with the radial position of the HFS probe. $\tau^{HFS}(peak)$ for the first few peaks is comparable to or larger than $\tau_{//}^{conv}(HFS\text{-}mid)$, for instance $\sim 50\,\mu s$ near the separatrix. This suggests that the ELM filaments are ejected into the HFS SOL during the early period of ELM instability, and that the radial extent of the filaments is restricted within the narrow region ($r^{mid} < 1$ cm) of the HFS SOL.

Another important finding is that $M_{//}^{HFS}(base)$ becomes $-0.1$ to $-0.4$, i.e., the flow reversal of the SOL plasma occurs over a wide SOL region ($r^{mid} < 4$ cm) after the appearance of the multiple peaks. This flow reversal is maintained during 0.5-1 ms, and may be caused by large out-gassing at the HFS divertor target due to the ELM heat load and large increase of fuel retention in the thick car-
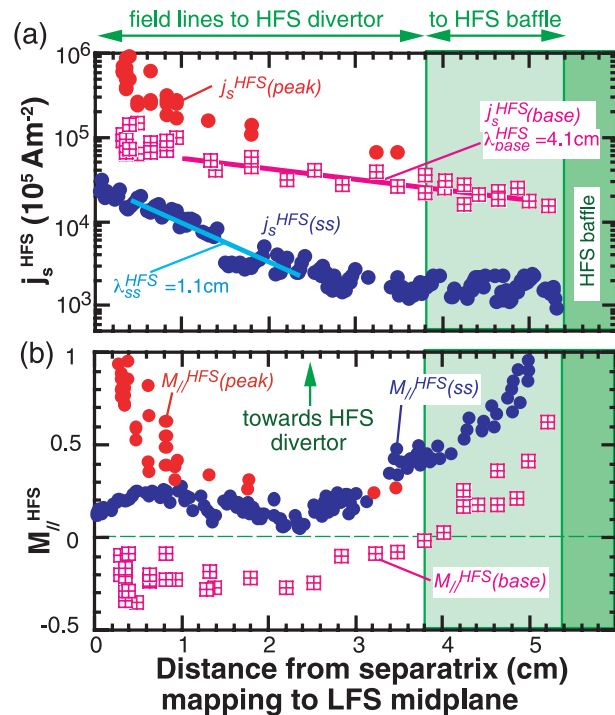


Fig. 9   Radial distributions of (a) $j_s^{HFS}$ peaks (red circles), maximum base-level (squares) during ELMs, and $j_s^{HFS}$ between ELMs (blue circles) measured at midplane-side of the HFS Mach probe, (b) Mach numbers corresponding to $j_s^{HFS}(peak)$, $j_s^{HFS}(base)$, $j_s^{HFS}(ss)$.
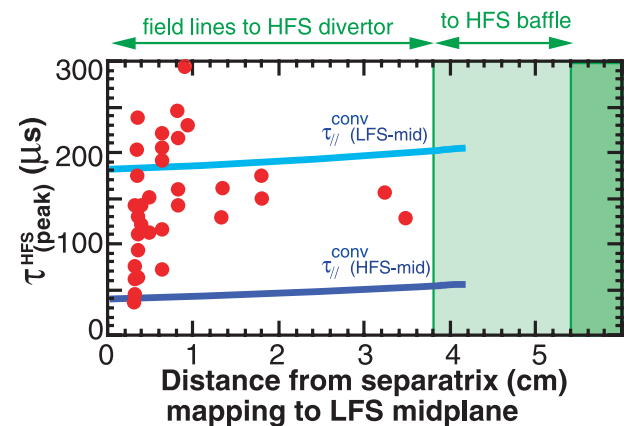


Fig. 10 Radial distributions of delay time of large multi-peaks (circles) and characteristic convection time from the LFS and HFS midplane to the HFS Mach probe, $\tau_{//}^{conv}(LFS\text{-}mid)$ and $\tau_{//}^{conv}(HFS\text{-}mid)$.

bon deposition layers between ELMs [30]. As a result, the plasma and impurity transport in the HFS SOL and divertor are influenced by the two transient convective fluxes during the ELM event—both can play important roles in the impurity deposition profiles.

# 4. Summary and Conclusion

Understanding of both steady-state and transient parallel flow patterns has progressed with the development of multi-point and fast sampling diagnostics, such as the Mach probes in the JT-60U L- and H-mode plasmas. Combined with the SOL flow measurements at different SOL locations, under various L-mode plasma conditions, such as density and plasma shape, common characteristics of the flow pattern were clarified. The subsonic level of the parallel SOL flow and in-out asymmetry in the fast SOL flow pattern are produced mainly by combination of driving mechanisms: (i) The in-out asymmetry in radial diffusion; (ii) classical drifts in a torus; and (iii) in-out asymmetry in the divertor plasma detachment. The effects of the toroidal field direction and density on the plasma flow can be explained.

Fast sampling of the ELMy H-mode plasma measurement shows that the dynamics of the parallel flow during ELM differed at the LFS and HFS SOLs. At the LFS SOL, convection transport to the divertor was dominant, which is consistent with the appearance of large $j_s^{mid}$ peaks, i.e., filaments are ejected, at the midplane SOL. At the same time, filaments lose the momentum of the pedestal rotation during ejection to the SOL, and their radial transport to the first wall is often faster than $\tau_{//}^{conv}$ to the divertor. At the HFS SOL, convection transport faster than the convective transport from the LFS midplane was often observed only near the separatrix ($r^{mid} < 1$ cm), suggesting that some filaments are ejected to the HFS. After the deposition of the convective flux, a dominant flow reversal was produced at the HFS divertor, possibly due to large neutral desorption from the target.

Both parallel and radial transport affects the SOL flow pattern and velocity. Quantitative determination of processes and modeling are necessary for operating a reactor such as ITER. The generation of the subsonic and sonic flows and the dynamics of the SOL plasma, including the plasma-wall interaction and atomic/molecular process will be required.

[1]  N. Asakura, J. Nucl. Matter. **363-365**, 41 (2007).
[2]  B. LaBombard et al., J. Nucl. Matter. **241-243**, 149 (1997).
[3]  N. Asakura et al., Nucl. Fusion **39**, 1983 (1999).
[4]  J.A. Boedo et al., J. Nucl. Matter. **266-269**, 783 (1999).
[5]  N. Asakura et al., Plasma Phys. Control. Fusion **44**, 2101 (2002).
[6]  S.K. Erents et al., Plasma Phys. Control. Fusion **46**, 1757 (2004).
[7]  B. LaBombard et al., Nucl. Fusion **44**, 1047 (2004).
[8]  R. Pitts et al., J. Nucl. Mater. **363-365**, 505 (2007).
[9]  H.W. Muller et al., J. Nucl. Mater. **363-365**, 605 (2007).
[10] J.P. Gunn et al., J. Nucl. Mater. **363-365**, 484 (2007).
[11] A. Loarte et al., Plasma Phys. Control. Fusion **44**, 1815 (2002).
[12] N. Asakura et al., Plasma Phys. Control. Fusion **44**, A313 (2002).
[13] A. Kirk et al., J. Phys. Conf. Ser. **123**, 012011 (2008).
[14] M. Tsalas et al., J. Nucl. Mater. **363-365**, 1095 (2007).
[15] I.H. Hutchinson, Phys. Rev. **A 37**, 4358 (1988).
[16] P.C. Stangeby and A.V. Chankin, Nucl. Fusion **36**, 839 (1996).
[17] A.V. Chankin and P.C. Stangeby, Plasma Phys. Control. Fusion **38**, 1879 (1996).
[18] N. Asakura et al., Phys. Rev. Lett. **84**, 3093 (2000).
[19] W. Fundamenski et al., J. Nucl. Matter. **337-339**, 305 (2005).
[20] A. Kirk et al., Phys. Rev. Lett. **92**, 245002 (2004).
[21] A. Herrmann et al., Plasma Phys. Control. Fusion **46**, 971 (2004).
[22] T. Eich et al., Plasma Phys. Control. Fusion **47**, 815 (2005).
[23] A. Kirk et al., Plasma Phys. Control. Fusion **47**, 315 (2005).
[24] J.A. Boedo et al., J. Nucl. Matter. **337-339**, 771 (2005).
[25] N. Asakura et al., J. Nucl. Matter. **337-339**, 712 (2005).
[26] M. Endler et al., Plasma Phys. Control. Fusion **47**, 219 (2005).
[27] J.A. Boedo et al., Phys. Plasmas **12**, 072516 (2005).
[28] R.A. Pitts et al., Nucl. Fusion **46**, 82 (2006).
[29] N. Asakura et al., J. Phys. Conf. Ser. **123**, 012009 (2008).
[30] Y. Ishimoto et al., J. Nucl. Matter. **350**, 301 (2006).